Ab initio potential for the He-Ag(110) interaction investigated using grazing-incidence fast-atom diffraction

C. A. Ríos Rubiano,[1] G. A. Bocan,[2] M. S. Gravielle,[1,*] N. Bundaleski,[3] H. Khemliche,[4] and P. Roncin[4]

[1]*Instituto de Astronomía y Física del Espacio, Consejo Nacional de Investigaciones Científicas y Técnicas, Universidad de Buenos Aires, Casilla de Correo 67, Sucursal 28, 1428 Buenos Aires, Argentina*

[2]*Centro Atómico Bariloche, Comisión Nacional de Energía Atómica and Consejo Nacional de Investigaciones Científicas y Técnicas, Av. Bustillo 9500, 8400 S.C. de Bariloche, Río Negro, Argentina*

[3]*CeFITec, Department of Physics, Faculdade de Ciências e Tecnologia, Universidade Nova de Lisboa, P-2829-516 Caparica, Portugal*

[4]*Institut des Sciences Moléculaires d'Orsay, ISMO, Centre National de la Recherche Scientifique-Université Paris-Sud, Unité Mixte de Recherches 8214, Bâtiment 351, Université Paris-Sud, 91405 Orsay Cedex, France*

(Received 25 October 2012; revised manuscript received 21 December 2012; published 18 January 2013)

Experimental diffraction patterns produced by grazing scattering of fast helium atoms from a Ag(110) surface are used as a sensitive tool to test an *ab initio* potential model derived from accurate density-functional theory (DFT) calculations. The scattering process is described by means of the surface eikonal approximation, which is a distorted-wave method that includes the quantum interference between contributions coming from different projectile paths, taking into account the complete corrugation of the three-dimensional projectile-surface potential. A fairly good agreement between the theoretical and experimental momentum distributions is found for incidence along different low-indexed crystallographic directions. This agreement is indicative of the quality of the DFT potential. The effective corrugation of the interaction potential across the incidence channel is also investigated.

DOI: 10.1103/PhysRevA.87.012903 PACS number(s): 79.20.Rf, 34.20.−b, 34.35.+a

I. INTRODUCTION

An accurate interaction potential for atom-surface systems is central for achieving a correct description of several processes and phenomena in surface science. This better understanding is in turn most relevant for technological applications, for example in the chemical industry. For the particular case of He-Ag systems, early semi-empirical potentials, as well as more recent ones based on *ab initio* calculations, have been proposed and probed by means of diverse physical properties, such as adsorption coefficients or scattering cross sections [1–4]. Regarding the phenomenon chosen to test the potential, two important aspects need to be considered: the energy range it can probe and its sensitivity to the characteristics of the model potential. In this respect, grazing-incidence fast-atom diffraction (GIFAD) on crystal surfaces has recently emerged as a powerful surface analysis method that allows one to probe surface interactions with an exceptional sensitivity in the 10 meV to few eV energy range [5–11].

A simple way of understanding the unexpected presence of interference signatures in the distributions of scattered atoms, after swift and grazingly impinging on a surface along low-indexed crystallographic directions [6], is to separately consider the fast movement of the projectile parallel to the incidence channel and its slow motion in the corresponding perpendicular plane. It was found that this particular geometrical condition helps to prevent the quantum decoherence originated by surface thermal vibrations [12,13], making it possible to observe GIFAD effects for a wide variety of materials. In fact, GIFAD patterns have been observed for insulator surfaces [5,6], where electronic excitations are strongly suppressed due to the presence of a wide band gap, but also for semiconductors [7], metals [14,15], as well as adsorbate-covered metal surfaces [16,17].

In this work we present both experimental data and theoretical results for projectile momentum distributions associated with grazing scattering of fast He atoms on a Ag(110) surface. This system corresponds to the first and simplest metallic case for which GIFAD effects were experimentally observed [14]. Here, we make use of the exceptional sensitivity of GIFAD patterns to the shape of the interaction potential to thoroughly check the quality of an *ab initio* He-Ag(110) potential.

We describe the He-Ag(110) interaction potential with a full three-dimensional (3D) potential energy surface (PES) that takes into account the projectile's three degrees of freedom. Such a 3D PES is obtained from an accurate density-functional theory (DFT) calculation derived with the QUANTUM ESPRESSO code [18], which is specially adequate to perform self-consistent calculations on metallic systems. We calculate a dense 3D grid of *ab initio* energies and obtain the complete 3D PES by means of a sophisticated interpolation technique [19].

The scattering process is evaluated within the surface eikonal (SE) approximation, which is a distorted wave method that makes use of the eikonal wave function to represent the elastic collision with the surface [20]. On the other hand, the motion of the fast projectile is classically described by considering axially channeled trajectories for different initial conditions. The SE approach is a semiclassical approximation that includes a clear description of the main mechanisms of the process. It has been successfully applied to investigate fast-atom diffraction from insulator surfaces [21–23]. In contrast to other approaches [24,25], the corrugation of the complete 3D PES is taken into account without averaging the projectile-surface potential along the incidence direction.

SE projectile distributions using the DFT potential are compared with the experimental spectra for helium incidence along three different directions of the Ag(110) surface: $[1\bar{1}0]$, [001], and $[1\bar{1}2]$. The paper is organized as follows. The

*Author to whom correspondence should be addressed: msilvia@iafe.uba.ar

experimental method and the theoretical model, including details of the potential evaluation, are summarized in Secs. II and III, respectively. Results are presented and discussed in Sec. IV, and in Sec. V we outline our conclusions. Atomic units (a.u.) are used unless otherwise stated.

II. EXPERIMENTAL METHOD

The experimental setup has been described in detail elsewhere [14]. A primary $^3He^+$ ion beam is extracted from an ECR ion source biased at the desired voltage, it is mass selected by a 180° magnet before being neutralized in a charge exchange chamber. The beam enters the UHV chamber, crosses the interaction region, and is imaged by a position-sensitive detector (PSD) located half a meter downstream on the opposite side of the chamber. A set of movable apertures is used to limit the atomic beam divergence down to the desired angular resolution as monitored on the PSD. Then, the Ag(110) surface is gradually inserted into the beam. The direct beam progressively disappears while the scattered particles appear around the direction corresponding to specular reflection on the surface. The Ag crystal is then rotated around the surface axis until the beam is aligned along a low-index crystallographic direction. The Ag(110) surface is prepared by cycles of large angle 500 eV Ar^+ sputtering, annealing at 600 °K and grazing angle sputtering by 5 keV Ar^+ ions. The Ag(110) crystal is then inserted almost parallel to the ^{3}He beam. The projectile total energy is tuned between 300 eV and 1 keV whereas the incidence angle is adjusted between 0.5 and 2 degrees, producing energies normal to the surface in the sub-eV range.

III. THEORETICAL MODEL

A. Surface eikonal approximation

Within the surface eikonal model the transition matrix per unit area $\mathcal{A}$ reads [20]

$$T_{if}^{(\mathrm{SE})} = \frac{1}{\mathcal{A}} \int_{\mathcal{A}} d\vec{R}_{\mathrm{os}}\, a_{if}(\vec{R}_{\mathrm{os}}), \tag{1}$$

where $\vec{R}_{\mathrm{os}}$ determines the initial position of the projectile on the surface plane and

$$a_{if}(\vec{R}_{\mathrm{os}}) = \frac{1}{(2\pi)^3} \int_{-\infty}^{+\infty} dt\ |v_z(\vec{\mathcal{R}}_P)| \times \exp[-i\,\vec{Q}.\vec{\mathcal{R}}_P - i\eta(\vec{\mathcal{R}}_P)]\ V_{\mathrm{SP}}(\vec{\mathcal{R}}_P) \tag{2}$$

is the transition amplitude associated with the classical path $\vec{\mathcal{R}}_P \equiv \vec{\mathcal{R}}_P(\vec{R}_{\mathrm{os}},t)$, with $v_z(\vec{\mathcal{R}}_P)$ the component of the projectile velocity perpendicular to the surface plane. In Eq. (2) $\vec{Q} = \vec{K}_f - \vec{K}_i$ denotes the projectile momentum transfer, with $\vec{K}_{i(f)}$ the initial (final) projectile momentum satisfying energy conservation (i.e., $K_f = K_i$). The phase η is the eikonal-Maslov phase, which is defined along the projectile path as [22]

$$\eta(\vec{\mathcal{R}}_P) = \int_{-\infty}^{t} dt'\ V_{\mathrm{SP}}(\vec{\mathcal{R}}_P(t')) + \phi_M, \tag{3}$$

where V_{SP} is the projectile-surface interaction and $\phi_M = \nu\pi/2$ is the Maslov correction term, with ν the Maslov index as defined in Ref. [26]. Note that the surface eikonal approach takes into account the quantum interference between transition amplitudes corresponding to different axially channeled projectile trajectories. Details on calculations are given in Refs. [20,22].

From Eq. (1), the transferred momentum distribution is obtained as

$$\frac{dP^{(\mathrm{SE})}}{dQ_{\mathrm{tr}}} = (2\pi)^4 m_P^2 \int d\theta_f\ \frac{\cos\theta_f}{\sqrt{K_{fs}^2 - Q_{\mathrm{tr}}^2}} \left|T_{if}^{(\mathrm{SE})}\right|^2, \tag{4}$$

where m_P is the projectile mass, $K_{fs} = K_f \cos\theta_f$ is the final momentum parallel to the surface, and $Q_{\mathrm{tr}} = K_f \cos\theta_f \sin\varphi_f$ is the transverse momentum transfer, that is, the component of $\vec{Q}$ perpendicular to the incidence channel on the surface plane, with θ_f and φ_f the exit polar and azimuthal angles, respectively.

B. Projectile-surface interaction

The interaction energy of the He atom with the Ag(110) surface is described with a full adiabatic 3D PES that depends on the atomic position $\vec{R}_P = (X,Y,Z)$. The PES is constructed from a grid of 252 *ab initio* energies over which an interpolation is performed.

All *ab initio* data are obtained from the DFT-based QUANTUM ESPRESSO code [18], which uses a plane-wave basis set to expand the system wave functions and is particularly efficient to model metallic surfaces. The values of relevant QUANTUM ESPRESSO parameters are chosen so that *ab initio* energies are calculated to a prescribed accuracy (differences <5 meV with respect to the converged result). The exchange-correlation energy is calculated within the generalized gradient approximation (GGA), using the Perdew-Burke-Ernzerhof energy functional (PBE) [27]. The electron-core interaction is described with ultrasoft pseudopotentials [28] (specifically, He.pbe-mt_fhi.UPF and Ag.pbe-d-rrkjus.UPF from www.quantum-espresso.org). The energy cutoff in the plane-wave expansion is 35.0 Ryd for the wave functions and 245.0 Ryd for the charge density and potential; the fractional occupancies are determined through the broadening approach of Marzari-Vanderbilt [29] with $\sigma = 0.01$ Ryd.; and the Brillouin-zone integration is performed with a $10 \times 7 \times 1$ Monkhorst-Pack grid of special k points, ensuring a k grid equally dense in all directions. The Ag lattice constant, obtained from a bulk calculation, is $a = 7.865$ a.u., this value being slightly higher than the experimental one (7.709 a.u.).

The Ag(110) surface is modeled by means of the supercell-slab scheme. A four-layer slab is used with a 2×2 cell in the plane parallel to the surface (atomic coverage of 0.25) and a supercell of length 25.03 a.u. along the normal to the surface ($\hat{z}$ axis). The latter length guarantees that the energy for He-Ag(110), with the He atom midway between slabs, is XY independent and thus provides a reasonable representation of the asymptotic region. This configuration, for which there is hardly any interaction with the surface, is chosen as the energy reference. In order to get the surface equilibrium geometry, the interlayer distance is relaxed from its bulk value $d_0 = 2.781$ a.u. The two bottom layers are kept fixed during the relaxation process, which continues until the energy difference between consecutive iterations is less than 10^{-4} a.u. and all

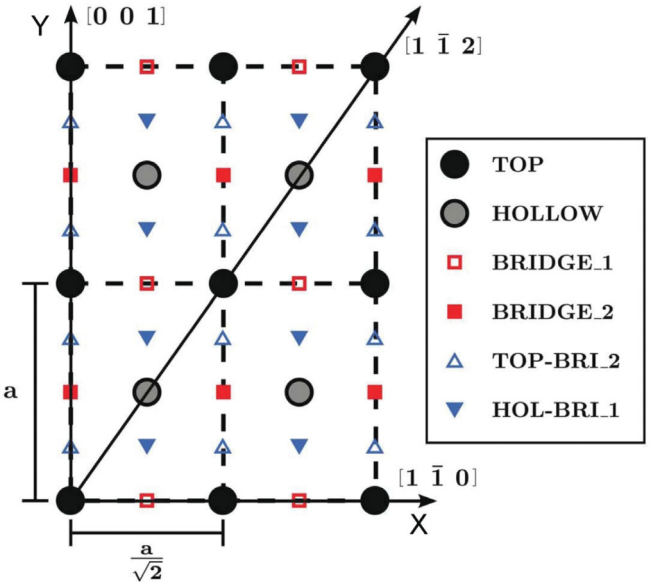

FIG. 1. (Color online) Depiction of the atomic positions of the Ag(110) surface, with a the lattice constant. The six (XY) sites shown in the figure correspond to the ones used for the PES calculation. Circles: TOP and HOLLOW sites standing for atoms of the first and second layers, respectively. Squares: BRIDGE_1 and BRIDGE_2 sites corresponding to the middle points between first and second TOP atomic neighbors, respectively. Triangles: middle points between the mentioned sites. The incidence directions of He atoms are also indicated.

components of all forces are less than 10^{-3} a.u. Geometry corrections due to relaxation amount to -9.14% and $+4.11\%$ for the first and second interlayer distances respectively, in accord with experimental results [30]. Once relaxed, the slab is kept frozen for the calculations that follow.

Given the closed-shell electronic structure of the He atom ($1s^2$), a non-spin-polarized calculation is enough for an adequate description of the ground state. A 3D energy grid is obtained. It consists of 42 equidistant points Z in the range $-2.0\,\text{a.u.} \leqslant Z \leqslant 8.25\,\text{a.u.}$, with $Z = 0$ corresponding to the topmost surface layer, and 6 sites [(X,Y) values] uniformly spread within the unit cell, as indicated in Fig. 1. Once the 252-point energy grid is derived, the corrugation reducing procedure [19] together with spline interpolation over the *ab initio* data are used to build the PES. Further details on the calculations are given in the Appendix. In Figs. 2(a) and 2(b) we show equipotential curves for two different distances to the surface, $Z = 3.0$ a.u. and $Z = 4.0$ a.u., respectively, corresponding to the characteristic region of He closest approach to the surface for the incidence conditions considered in this work.

IV. RESULTS

In this article, experimental momentum distributions of ^{3}He atoms scattered from a Ag(110) surface under grazing-incidence conditions are employed in order to probe the DFT potential energy surface. The evaluation of the SE transition matrix from Eq. (1) involves the integration on the initial position $\vec{R}_{\text{os}}$ of the classical trajectory on a given area $\mathcal{A}$.

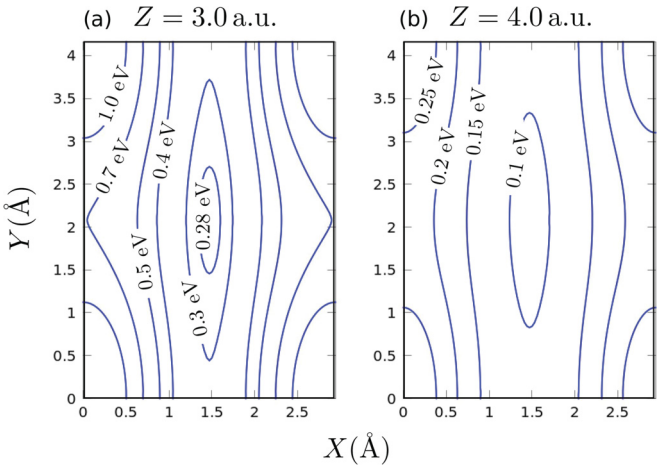

FIG. 2. (Color online) Equipotential curves for the interaction between the He atom and the Ag(110) surface, as a function of the coordinates X and Y, along the [1$\bar{1}$0] and [001] directions, respectively. Two different distances to the surface are considered: (a) $Z = 3.0$ a.u., and (b) $Z = 4.0$ a.u.

This integral was calculated with the Monte Carlo technique using more than 2×10^5 classical trajectories, with random $\vec{R}_{\text{os}}$ values given by a Gaussian distribution, which avoids the unphysical interferences that arise in the momentum spectra when uniform random positions are used.

We start by considering incidence along the [1$\bar{1}$0] channel, which presents the strongest corrugation and, consequently, the richest diffraction patterns. In order to provide an overall understanding of the GIFAD scenario, in Fig. 3 we compare experimental and theoretical diffraction charts for ^{3}He atoms impinging on the silver surface with an energy $E = K_i^2/(2m_P) = 0.5$ keV. Such diffraction charts display the intensity of the projectile distribution as a function of the transverse transferred momentum Q_{tr} and the normal impact energy $E_\perp = E \sin^2\theta_i$, where θ_i denotes the incidence angle measured with respect to the surface plane. Note that different values of $E_\perp$ allow one to probe potential contours across the incidence direction for different distances to the surface. Therefore, the general good agreement between the experimental and simulated two-dimensional diffraction charts of Fig. 3 is a signature of the quality of the present DFT potential in the 0.05–0.3 eV range of perpendicular energies.

A closer examination of Fig. 3 reveals a series of maxima and minima structures in the SE diffraction chart, which are symmetrically placed with respect to the incidence direction, for which $Q_{\text{tr}} = 0$. Similar patterns are also present in the experimental distribution, which displays a slight momentum asymmetry attributed to a small misalignment of the incident beam with respect to the low-indexed crystallographic direction. As it is the case with all diffraction techniques, these interference structures stem from two different contributions, the structure factor, responsible for the presence of the Bragg peaks, and the form factor, responsible for the intensity variations. Both mechanisms can be separately analyzed within the SE model by factorizing the transition matrix as [23]

$$T_{if}^{(\text{SE})} = \widetilde{T}_1^{(\text{SE})}(Q_{\text{tr}})\, S_{n_{\text{tr}}}(Q_{\text{tr}}), \tag{5}$$

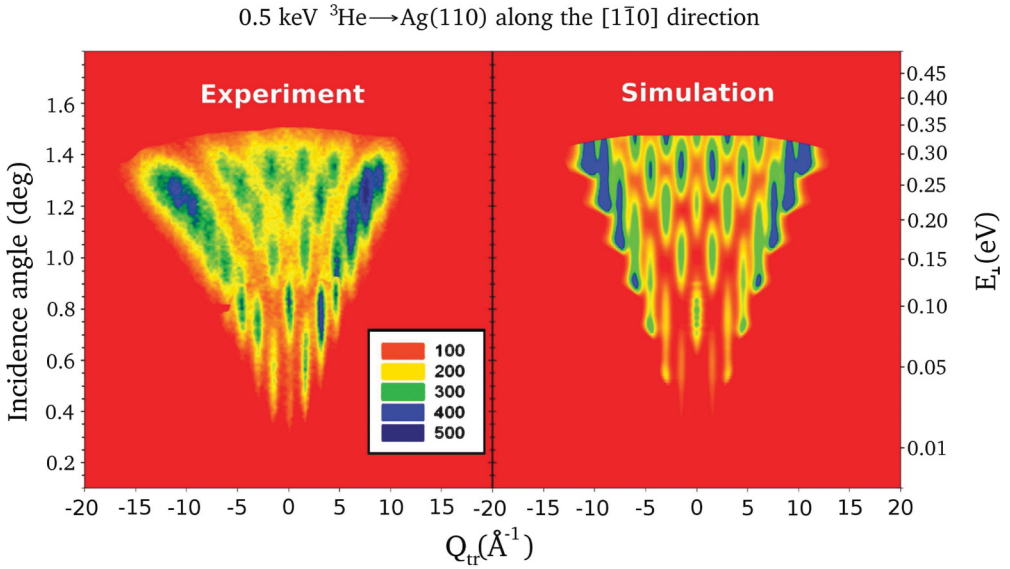

FIG. 3. (Color online) Two-dimensional diffraction chart displaying (a) experimental intensities and (b) SE differential momentum probabilities, as a function of the normal energy $E_\perp$ and the transverse momentum transfer $Q_{\rm tr}$, for 0.5 keV ^{3}He atoms impinging along the [1$\bar{1}$0] direction.

where $\widetilde{T}_1^{(\rm SE)}(Q_{\rm tr})$ is derived from Eq. (1) by evaluating the $\vec{R}_{\rm os}$ integral over *one* reduced unit cell. For incidence along the [1$\bar{1}$0] and [001] channels, the second factor reads $S_{n_{\rm tr}}(Q_{\rm tr}) = \sin(n_{\rm tr}\,\beta)/(n_{\rm tr}\sin\beta)$, where $n_{\rm tr}$ denotes the number of reduced unit cells along the transverse direction that are included in the integration region $\mathcal{A}$, and $\beta = Q_{\rm tr}\,d/2$, with d the spacial periodicity of the channel. The $S_{n_{\rm tr}}(Q_{\rm tr})$ factor is due to interference between projectile trajectories whose initial positions are separated by a distance just equal to d and gives rise to Bragg peaks placed at $Q_{\rm tr} = m2\pi/d$, with m an integer number. From Eq. (5), the intensities of such Bragg maxima are completely determined by the envelope factor, $\widetilde{T}_1^{(\rm SE)}$. The $\widetilde{T}_1^{(\rm SE)}(Q_{\rm tr})$ factor is the result of the interference between projectile trajectories whose initial positions are separated by a distance smaller than d and presents an oscillatory structure as a function of $Q_{\rm tr}$, which is associated with the projectile deflection by the surface potential. When a large number of diffraction orders is observed, these oscillatory structures are sometimes called supernumerary rainbows [25]. Thus, Bragg peak positions provide information about the crystallographic structure only, but their intensities are extremely sensitive to the shape of the PES across the incidence channel. What is more, it was found that small changes in the surface potential can modify strongly the supernumerary rainbow factor, even transforming a GIFAD maximum into a minimum [21,24].

In Fig. 4 we plot experimental and theoretical GIFAD patterns for 0.5 keV He atoms impinging along the [001] direction. Perpendicular energies in the range from 0.20 to 0.32 eV are considered. In the figure, SE differential probabilities obtained by considering an integration region $\mathcal{A}$ equal to 8×8 reduced unit cells are displayed with a blue dashed line. These results present narrow Bragg maxima, whose positions are indicated with vertical dashed lines in the figure. Note that the width of these Bragg peaks is governed by $n_{\rm tr}$ (in our case, $n_{\rm tr} = 8$), and it gets smaller as $n_{\rm tr}$ increases. On the other hand, since the factor $\widetilde{T}_1^{(\rm SE)}$ determines the number of observed Bragg maxima, the smaller corrugation of this crystallographic channel results in narrower spectra than the ones of Fig. 3 for the same normal energies.

In order to simulate the experimental conditions and establish a comparison with experimental data, in Fig. 4 we also plot SE differential probabilities convoluted with a Lorentz function (blue solid line), where the parameters of the line broadening were obtained from the observed

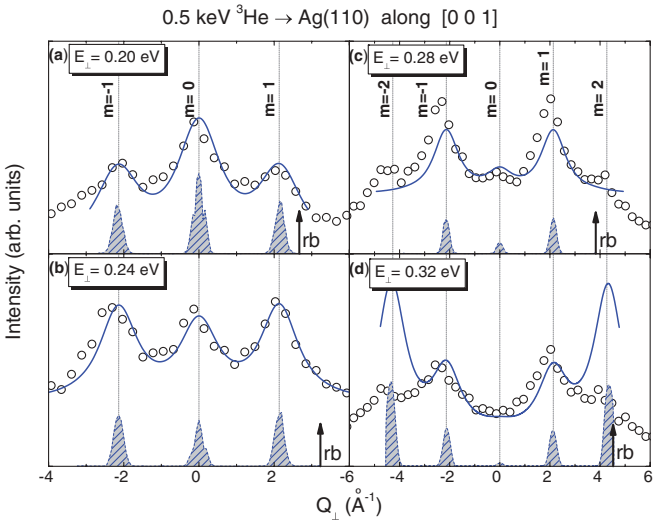

FIG. 4. (Color online) Momentum distributions, as a function of the transverse momentum transfer $Q_{\rm tr}$, for 0.5 keV ^{3}He atoms impinging on Ag(110) along the [001] direction. The normal incidence energy is: (a) 0.20 eV, (b) 0.24 eV, (c) 0.28 eV, and (d) 0.32 eV. Empty circles: experimental data. Solid blue line: SE differential probability convoluted to include inherent uncertainties. Dashed blue line: SE differential probabilities without convolution, as explained in the text. The vertical dashed lines show Bragg peak positions and the arrow indicates the position of the classical rainbow maximum.

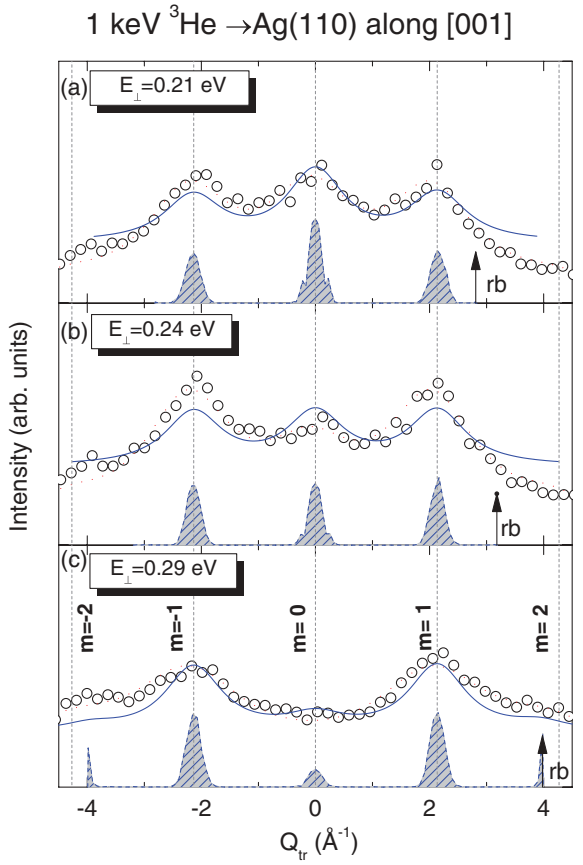

FIG. 5. (Color online) Similar to Fig. 4 for 1 keV ^{3}He atoms impinging along the [001] direction. The normal incidence energy is: (a) 0.21 eV, (b) 0.24 eV, and (c) 0.29 eV.

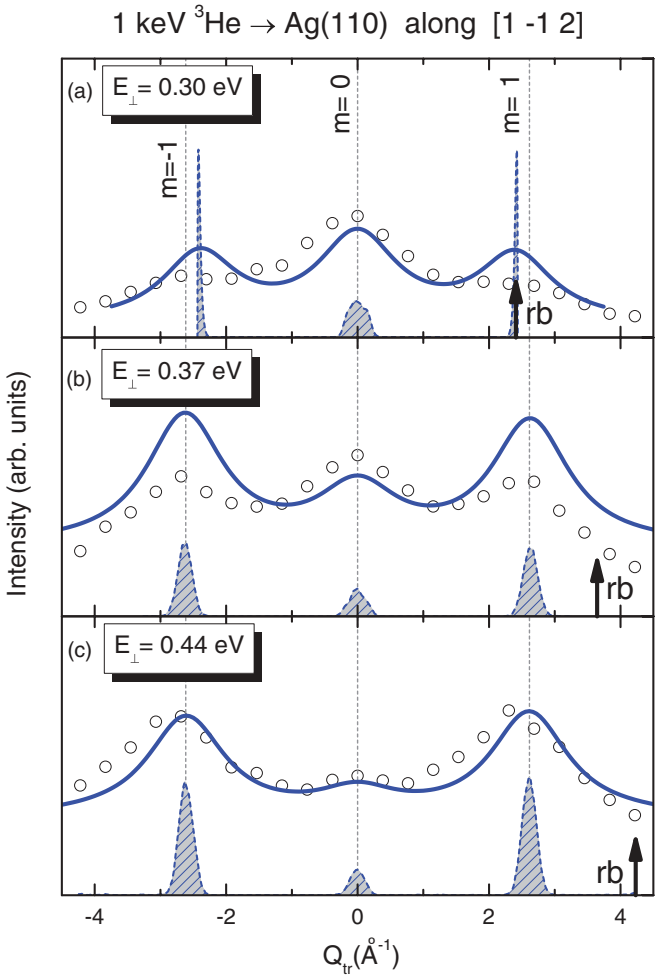

FIG. 6. (Color online) Similar to Fig. 4 for 1 keV ^{3}He atoms impinging along the [1$\bar{1}$2] direction with normal incidence energy (a) 0.30 eV, (b) 0.37 eV, and (c) 0.44 eV.

linewidths [14]. This convolution takes into account not only the experimental divergence of the incident beam but also the broadening introduced by both thermal vibrations of lattice atoms and inelastic processes, which contribute to deteriorate the coherence [31]. We find a fairly good agreement between convoluted SE results and experimental intensities, with the exception of the Bragg maxima of order $m = \pm 2$ for $E_\perp = 0.32$ eV, whose intensities are overestimated by the SE curve. This fact is related to the presence of sharp rainbow peaks in the $\widetilde{T}_1^{(\mathrm{SE})}$ function, which are originated by the classical description of the projectile motion [32]. Such rainbow peaks affect the outermost Bragg maxima when they are close to each other, as observed in Fig. 4(d), but this deficiency does not have any influence on the SE distribution at smaller deflection angles.

In Fig. 5, experimental momentum spectra for 1 keV He atoms impinging on a silver surface along the [001] direction are compared with SE distributions obtained both including and not including the convolution. As reported in previous works [21,24], the intensity of the central peak, corresponding to the Bragg maximum of order $m = 0$, is extremely sensitive to the corrugation amplitude of the surface potential. In a simple Hard-Wall model this trough to peak amplitude is called h and the intensity of the Bragg maximum of order $m = 0$ oscillates with the geometrical phase $\Phi = K_{i\perp} h$, where $K_{i\perp} = K_i \sin\theta_i$ is the initial projectile momentum perpendicular to the surface [33]. This means that the corrugation amplitude h is probed with an accuracy, which is a fraction of the perpendicular wavelength. In the figure we observe how a small variation in the $E_\perp$ value strongly modifies the relative intensity of the zeroth-order Bragg peak, which switches from being almost an absolute maximum for $E_\perp = 0.21$ eV to a minimum for $E_\perp = 0.29$ eV. This behavior is well reproduced by the simulations based on the DFT potential, indicating that the *ab initio* model gives an appropriate description of the He-Ag(110) interaction in this normal energy range.

To complete the analysis of the surface potential we consider an He beam impinging along the [1$\bar{1}$2] channel with $E = 1$ keV. In Fig. 6 experimental momentum distributions for normal energies ranging from 0.30 to 0.44 eV are compared with convoluted and unconvoluted SE spectra. For $E_\perp = 0.44$ eV [Fig. 6(c)] we find that the SE momentum spectrum, including experimental and inherent uncertainties through convolution, is in very good agreement with the experimental data in the whole Q_{tr} range. But, since the Q_{tr} position of the classical rainbow peak depends on $E_\perp$, when the normal energy decreases and the classical rainbow maximum becomes close to the outermost Bragg position, as observed from the unconvoluted values of Fig. 6(a), the

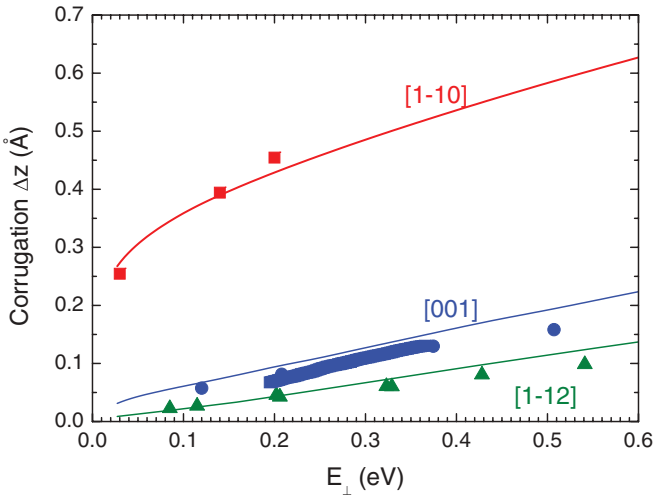

FIG. 7. (Color online) Effective corrugation Δz of the potential across the low-indexed crystallographic channels $[1\bar{1}0]$, [001], and $[1\bar{1}2]$, as a function of the perpendicular energy. Full symbols, experimentally derived results in Hard-Wall approximation; solid curves, values derived from the present DFT potential.

corresponding Bragg intensity starts to be overestimated. However, as explained above, this failure is a characteristic of the semiclassical methods and it is not related to the potential model. Furthermore, taking into account that the number of observed Bragg maxima depends strongly on the shape of the equipotential curves across the incidence channel [24], the general agreement between the experimental and simulated diffraction spectra of Fig. 6 can be considered as an indication of the performance of the present DFT potential in such a perpendicular energy range.

Finally, in Fig. 7 we plot the effective corrugation Δz of the potential across the different channels, $[1\bar{1}0]$, [001], and $[1\bar{1}2]$, as a function of the perpendicular energy $E_\perp$. The corrugation Δz is defined as the normal distance between the maximum and the minimum of an equipotential surface that is obtained by averaging the 3D PES along the incidence direction. Experimentally derived data, displayed with full symbols in the figure, were deduced from Bragg peak intensities under different angles of incidence by using the Hard-Wall model [33]. In all the cases considered the theoretical curve is close to the experimentally derived data, showing an increase of the corrugation with the normal energy, in opposition to what happens for the LiF(001) surface along the [110] direction [22].

V. CONCLUSION

We have addressed, both experimentally and theoretically, GIFAD patterns for He atoms scattered from a Ag(110) surface in order to probe an *ab initio* surface potential that was obtained from DFT by making use of the QUANTUM ESPRESSO code. Momentum distributions of scattered projectiles were derived from the SE approximation, which takes into account the quantum interference in terms of the coherent superposition of transition amplitudes for different projectile paths with the same final momentum.

SE results for incidence along three different crystallographic directions of the Ag(110) surface are compared with experimental data considering a wide range of energies associated with the motion normal to the surface plane. Several aspects of the experimental momentum distributions are well reproduced by the theoretical simulations. Taking into account the extreme sensitivity of fast atom diffraction patterns, we thus conclude that the present *ab initio* DFT surface potential provides an appropriate description of the He-Ag(110) interaction for perpendicular energies in the $E_\perp =$ 0.1 eV–0.5 eV range. In addition, we have investigated the effective corrugation across the different incidence channels, as a function of the perpendicular energy, finding good agreement with the experimentally derived corrugation.

ACKNOWLEDGMENTS

C.R.R. and M.S.G. acknowledge financial support by CONICET, UBA, and ANPCyT of Argentina. M.S.G. would like to express gratitude to the Université Paris-Sud for support during a portion of this work. G.A.B. acknowledges financial support by ANPCyT and is also thankful to H. F. Busnengo, J. D. Führ, and M. L. Martiarena regarding the PES calculation. The experimental work was supported by the ANR under Contract No. ANR-07-BLAN-0160-01.

APPENDIX: ON THE HE-AG(110) INTERACTION POTENTIAL PRECISION

In this Appendix we present supplementary information on the interaction potential used in this work. Figure 8 shows the *ab initio* energies as a function of Z, for the six XY grid sites (Fig. 1). As it was pointed out in the main text, these calculations were performed for a set of parameters carefully chosen so that the energy differences were well converged within a 5 meV margin. Mark the energy's XY asymptotic independence (see Fig. 8 inset), which is indicative of an enough amount of vacuum between slabs.

Once the XYZ grid is obtained, the corrugation reducing procedure together with spline interpolation are used to build up the PES as a function of the He atom XYZ coordinates. Within this scheme, the quality of the interpolation will be

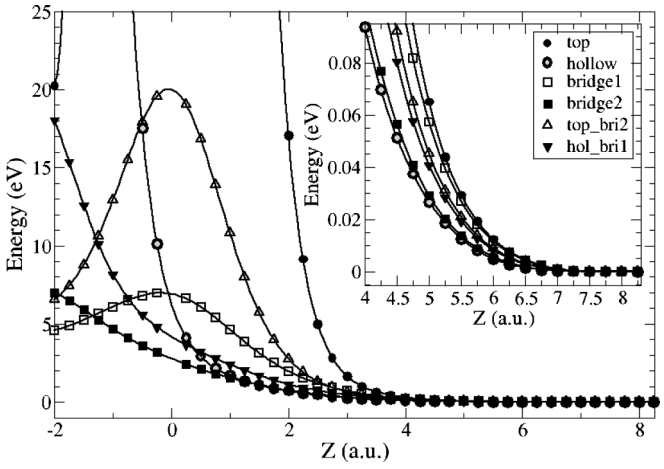

FIG. 8. Energy vs Z for the six XY sites used to make the interpolation grid. $Z = 0$ corresponds to the position of the topmost atomic layer of the Ag(110) surface. A detail of the asymptotic region is shown in the inset.

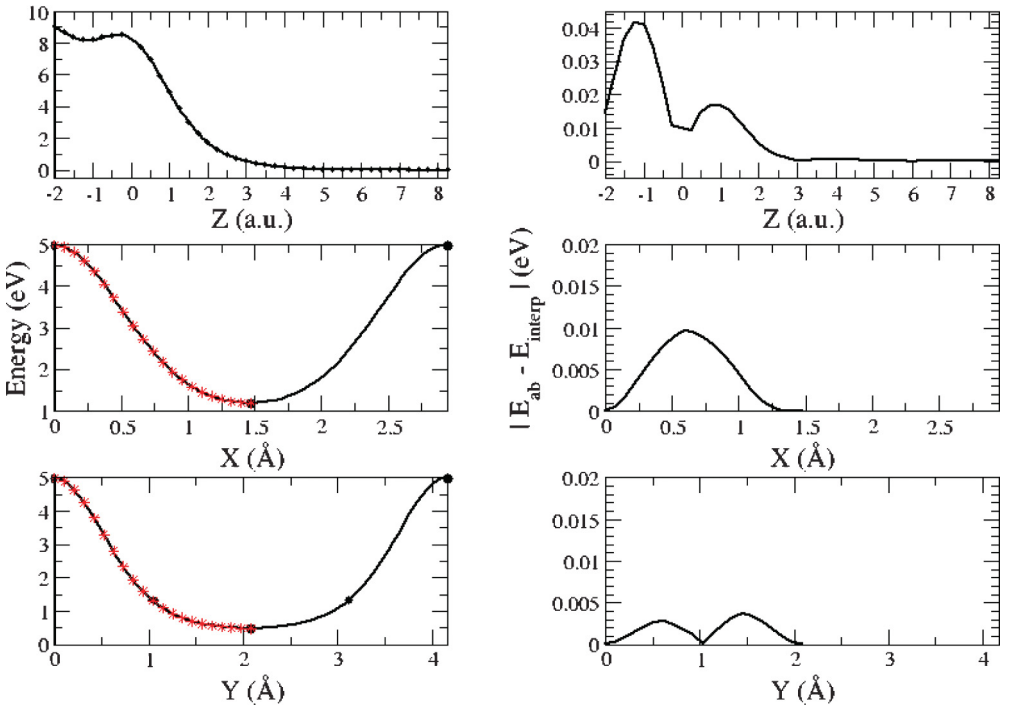

FIG. 9. (Color online) Interpolation checks. Full circles, *ab initio* data used in the interpolation; red crosses, *ab initio* data used to test the interpolation procedure. Top: Energy (left) and difference between interpolated and *ab initio* energy (right), as a function of Z, for the off-grid top-hollow site, located at mid-distance between a TOP and a HOLLOW site. Middle: Energy (left) and difference between interpolated and *ab initio* energy (right), as a function of X, for $Z = 2.5$ a.u. ~ 1.3 Å and $Y = 0$. Bottom: Energy (left) and difference between interpolated and *ab initio* energy (right), as a function of Y, for $Z = 2.5$ a.u. ~ 1.3 Å and $X = 0$.

affected by the grid density, particularly the XY one. Given the symmetry and geometry of Ag(110), the six XY sites used allow us to build a 3×5 point grid with an approximately uniform distribution (see Fig. 1 in the main text).

The quality of the interpolation is checked by contrasting interpolated to test *ab initio* calculations for off-grid trajectories along X, Y, and Z. The results are shown in Fig. 9. On analyzing this figure we must keep in mind that the region closest to the surface, being the one with the highest corrugation, is also the most challenging region for the interpolation. Therefore, in the middle and bottom panels we have considered trajectories along the $[1\bar{1}0]$ and [001] directions for a fixed in-grid $Z = 2.5$ a.u. ~ 1.3 Å. The differences observed (right column) are all below 10 meV. Regarding this result, note that for every dynamic simulation performed in this work the closest distance to the surface reached by the He atoms was $Z_{\min} \gtrsim 2.8$ a.u., where the interpolation will perform even better than at the tested distance. In the top panel of Fig. 9 we have considered a trajectory along Z for an off-grid site, corresponding to the midpoint between a TOP and HOLLOW site. We see here that in the Z region of interest for the dynamics, the differences between interpolated and *ab initio* results are around a few meVs.

Finally, we reckon it worth mentioning that the DFT calculation 5 meV convergence margin or the interpolation error do not by themselves represent how well the PES will compare to experimental data. There are several other factors that might affect the PES precision. The forced periodicity of the supercell-slab scheme, the approximation used to include exchange correlation energy in the DFT calculation or the neglect of Van der Waals interactions, although not expected to play an important role in the process under study, are other sources of error to keep in mind.

[1] A. Luntz, L. Mattera, M. Rocca, F. Tommasini, and U. Valbusa, Surf. Sci. **120**, L447 (1982).
[2] R. Schinke and A. C. Luntz, Surf. Sci. Lett. **124**, L60 (1983).
[3] V. Celli, G. Benedek, U. Harten, J. P. Toennies, R. B. Doak, and V. Bortolani, Surf. Sci. **143**, L376 (1984).
[4] M. G. Dondi, L. Mattera, S. Terreni, F. Tommasini, and U. Linke, Phys. Rev. B **34**, 5897 (1986).
[5] A. Schüller, S. Wethekam, and H. Winter, Phys. Rev. Lett. **98**, 016103 (2007).
[6] P. Rousseau, H. Khemliche, A. G. Borisov, and P. Roncin, Phys. Rev. Lett. **98**, 016104 (2007).
[7] H. Khemliche, P. Rousseau, P. Roncin, V. H. Etgens, and F. Finocchi, Appl. Phys. Lett. **95**, 151901 (2009).
[8] H. Winter, J. Seifert, D. Blauth, M. Busch, A. Schüller, S. Wethekam, Appl. Surf. Sci. **256**, 365 (2009).

[9] A. Momeni, P. Soulisse, P. Rousseau, H. Khemliche, and P. Roncin, e-J: Surf. Sci. Nanotech. **8**, 101 (2010).
[10] J. Seifert, A. Schüller, H. Winter, R. Wlodarczyk, J. Sauer, and M. Sierka, Phys. Rev. B **82**, 035436 (2010).
[11] H. Winter and A. Schüller, Prog. Surf. Sci. **86**, 169 (2011), and references therein.
[12] P. Rousseau, H. Khemliche, N. Bundaleski, P. Soulisse, A. Momeni, and P. Roncin, J. Phys.: Conf. Ser. **133**, 012013 (2008).
[13] J. R. Manson, H. Khemliche, and P. Roncin, Phys. Rev. B **78**, 155408 (2008).
[14] N. Bundaleski, H. Khemliche, P. Soulisse, and P. Roncin, Phys. Rev. Lett. **101**, 177601 (2008).
[15] M. Busch, A. Schüller, S. Wethekam, and H. Winter, Surf. Sci. **603**, L23 (2009).
[16] A. Schüller, M. Busch, S. Wethekam, and H. Winter, Phys. Rev. Lett. **102**, 017602 (2009).
[17] J. Seifert and H. Winter, Phys. Rev. Lett. **108**, 065503 (2012).
[18] P. Giannozzi *et al.*, J. Phys.: Condens. Matter **21**, 395502 (2009).
[19] H. F. Busnengo, A. Salin, and W. Dong, J. Chem. Phys. **112**, 7641 (2000).
[20] M. S. Gravielle and J. E. Miraglia, Phys. Rev. A **78**, 022901 (2008).
[21] M. S. Gravielle and J. E. Miraglia, Nucl. Instrum. Meth. Phys. Res. B **267**, 610 (2009).
[22] A. Schüller, H. Winter, M. S. Gravielle, J. M. Pruneda, and J. E. Miraglia, Phys. Rev. A **80**, 062903 (2009).
[23] M. S. Gravielle, A. Schüller, H. Winter, and J. E. Miraglia, Nucl. Instrum. Meth. Phys. Res. B **269**, 1208 (2011).
[24] F. Aigner, N. Simonović, B. Solleder, L. Wirtz, and J. Burgdörfer, Phys. Rev. Lett. **101**, 253201 (2008).
[25] A. Schüller and H. Winter, Phys. Rev. Lett. **100**, 097602 (2008).
[26] W. F. Avrin and R. P. Merrill, Surf. Sci. **311**, 269 (1994).
[27] J. P. Perdew, K. Burke, and M. Ernzerhof, Phys. Rev. Lett. **77**, 3865 (1996).
[28] D. Vanderbilt, Phys. Rev. B **41**, 7892 (1990).
[29] N. Marzari, D. Vanderbilt, A. De Vita, and M. C. Payne, Phys. Rev. Lett. **82**, 3296 (1999).
[30] B. W. Busch and T. Gustafsson, Surf. Sci. **407**, 7 (1998); M. Lindroos *et al.*, *ibid*. **218**, 269 (1989); E. Holub-Krappe *et al.*, *ibid.* **188**, 335 (1987); Y. Kuk and L. C. Feldman, Phys. Rev. B **30**, 5811 (1984).
[31] In order to account for the incoherent background observed in the experiment, a constant term was also added to the convoluted SE probabilities.
[32] M. V. Berry and K. E. Mount, Rep. Prog. Phys. **35**, 315 (1972).
[33] U. Garibaldi, A. C. Levi, R. Spadacini, and G. E. Tommei, Suf. Sci. **48**, 649 (1975).